Measurement of energy and angular distributions of secondary ions in the sputtering of gold by swift Au_n clusters: Study of emission mechanisms

S. Bouneau,[1] S. Della Negra,[1] D. Jacquet,[1] Y. Le Beyec,[1] M. Pautrat,[1] M. H. Shapiro,[2,3] and T. A. Tombrello[3]
[1]*Institut de Physique Nucléaire, IN2P3-CNRS and Université Paris XI-Sud, F-91406 Orsay cedex, France*
[2]*Department of Physics, California State University, P.O. Box 6866, Fullerton, California 92834-6866, USA*
[3]*Division of Physics, Mathematics and Astronomy, California Institute of Technology, Pasadena, California 91125, USA*
(Received 18 October 2004; revised manuscript received 31 January 2005; published 24 May 2005)

Energy and angular distributions of negative ions (Au^-, Au_2^-, Au_3^-, and Au_5^-) emitted from gold target bombarded by Au, Au_4, and Au_9 projectiles at 200 keV/atom were measured with a multipixel position sensitive detector. The angular distributions are symmetrical with respect to the normal to the target surface and forward peaked. They depend on the type of emitted ions, on the emission energy, and on the projectile size. More forward directed emission is observed with Au_9 projectiles. The secondary ion energy distributions obtained with Au and Au_4 projectiles are well reproduced by a sum of linear collision cascades and thermal spike processes. However, in the case of Au_9 projectiles the energy distributions are better described by using a simple spike model with two different average temperature regimes: the first one corresponds to high emission energy occurring in the early stage of the whole process, and the second to the low energy component.

DOI: 10.1103/PhysRevB.71.174110 PACS number(s): 79.20.Rf, 36.40.−c, 29.40.Gx, 68.49.Sf

I. INTRODUCTION

For many years, beams of gold clusters Au_n with a number n of constituents between 2 and several hundreds have been produced in our laboratory at energies per atom from tens of eV to tens of MeV. Several regimes of energy loss in the collision of these clusters with solids have been investigated. In particular, a sputtering study of gold material by Au_n clusters ($n=2-13$) at energy per atom between 20 keV and 3 MeV[1,2] revealed the existence of an important maximum of sputtering yield at about 200 keV/atom. For example, an unexpectedly high sputtering yield of more than 15 000 gold atoms emitted per single impact of Au_{13} was measured. At the surface of the gold target craters with diameter as large as 250 Å were observed showing that important surface modification takes place during sputtering. Large nonequilibrium processes thus are obviously involved in such "giant sputtering events" and comparisons with analytical models do not straightforwardly explain the large yield values and their variation with cluster incident energy.

In an attempt to obtain more information on the possible mechanisms, measurements of angular and energy distributions of the emitted secondary ions were performed with three different projectiles Au, Au_4, and Au_9 at 200 keV/atom bombarding a gold target. A multiparameter detection system allowed us—by coincidence data analysis—to identify the emitted ions and to correlate their emission angle and energy.

Recent molecular dynamic (MD) simulations with Au_n bombarding polycrystalline gold target have been performed at 16 keV/atom by Colla and Urbassek[3] and at 100 keV/atom by Shapiro and Tombrello.[4] In both simulations, it is demonstrated that emission of the most energetic particles takes place within the first picosecond. The high deposited energy density by the cluster projectile is first dissipated by collision cascades that cause disruption of the surface and emission of fast atoms and clusters. A long phase of thermal emission takes place afterwards with a temporal evolution that depends on the incident cluster size and energy. This is well illustrated in Ref. 4 with Au_2 projectiles used to calculate angular and energy distributions at different times after the impact which are then compared with standard Thompson[5] and Sigmund-Claussen distributions.[6] The physical parameters of these distributions, the surface binding energy U_b and the effective temperature kT, are found to change as a function of time. Since experimental access to emission time sequences is not possible, we have applied a fitting procedure to the measured distributions of various emitted ions by assuming that the two processes of linear collision cascades (LC) and thermal spike (TS) are both contributing to the entire spectra. The secondary ion energy distributions obtained with Au and Au_4 projectiles are very well described within this approach. However, for Au_9 projectiles the secondary ion emission cannot be described satisfactorily through LC and a TS process with a single mean temperature. For this case, we propose a more realistic alternative based on a spike process with two regimes of average temperature.

In this paper we present the experimental method to determine times of flight and emission angles of secondary ions detected by a 256 pixelated channel plate detector followed by the procedure that is applied to obtain the energy and angular distributions. The event by event data acquisition mode allows us to set intervals of secondary ion energy and angle in order to provide more precise information on the emission mechanisms. The comparison of the gated experimental distributions with different models is then discussed.

II. EXPERIMENTAL SETUP AND ANALYSIS PROCEDURE

In the following, we describe an experimental method to determine event by event the kinematical characteristics of

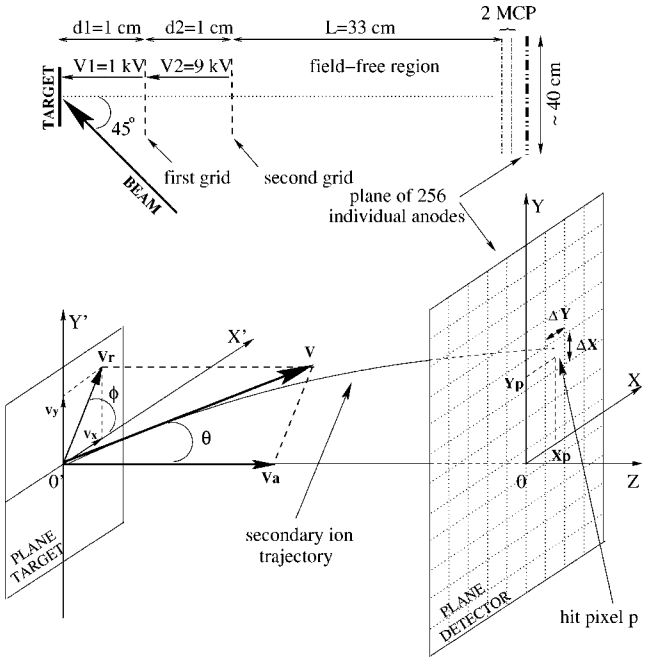

FIG. 1. Top, schematic arrangement of target, acceleration grids, and multipixel detector. The experimental parameters d_1, d_2, L, V_1, and V_2 defined in Sec. II A are also indicated. Bottom, representation of the kinematical quantities, total emission velocity V, axial velocity V_a and radial velocity V_r, polar and azimuthal angles θ and ϕ. A secondary ion trajectory is shown and the center coordinates (X_p, Y_p) of the hit pixel p are defined with respect to the detector center O. Each pixel has an area of $(\Delta X \times \Delta Y)$.

each secondary ion emitted under a projectile impact on a solid target in order to obtain, over a large number of events, their energy and angular distributions.

The measurement of secondary ion emission velocity is based on a linear time of flight technique coupled to a multi-impact position sensitive stop detector. Two acceleration grids in front of the target allow us to apply homogeneous and constant electric fields perpendicularly to the target plane. In this configuration, the secondary ion time of flight measured between the target and the detector depends only on the axial velocity, V_a, defined as the emission velocity projection onto the normal to the target surface (see Fig. 1). Simultaneously, the position of the secondary ion impact on the detector surface, parallel to the target, gives access to the radial velocity V_r, the emission velocity projection onto the target plane (see Fig. 1). The polar angle θ, which represents the emission direction with respect to the normal to the target surface, is then defined by

$$\tan\theta = \frac{V_r}{V_a}. \tag{2.1}$$

From the two components V_X and V_Y of the radial velocity into the target plane, the azimuthal angle ϕ is expressed as

$$\tan\phi = \frac{V_Y}{V_X}. \tag{2.2}$$

These quantities and the geometrical arrangement of the target and the stop detector are shown in Fig. 1.

Beams of gold clusters were accelerated by the Orsay tandem accelerator which is equipped with a cluster liquid metal ion source at the high voltage terminal.[7–9] Gold targets (thickness of about 1000 nm) were prepared by vapor deposition on thick stainless steel foils, and bombarded by the Au_n cluster beam at an angle of 45° with respect to the normal to the target surface. The beam size was defined by horizontal and vertical slits which were mechanically adjusted to an aperture of 300 μm $\times$ 300 μm. The rate was about 100 projectiles/s. The beam was pulsed to give a start signal for the acquisition system.

The detector used in this work is a 256-anode channel plate device which is fully described in Ref. 10. There are 256 independent electronic channels providing 256 time of flight mass spectra with the same start signal. The size of one pixel is 2.54 mm $\times$ 2.54 mm and the time encoding is achieved in a time bin of 0.5 ns. This detector is well adapted to detect simultaneously a large number of different secondary ions which are generated by impact of large cluster projectiles.

A. Time-of-flight measurement and axial energy determination

The axial energy E_a of a secondary ion with a mass m and a charge q is obtained from the measurement of its time of flight (TOF) t by the relation

$$t = \sqrt{2m}\left[\frac{d_1}{\sqrt{qV_1}}\left(-\sqrt{\frac{E_a}{qV_1}}+\sqrt{1+\frac{E_a}{qV_1}}\right)\right.$$
$$+\frac{d_2}{\sqrt{qV_2}}\left(-\sqrt{\frac{E_a}{qV_2}+\frac{V_1}{V_2}}+\sqrt{1+\frac{E_a}{qV_2}+\frac{V_1}{V_2}}\right)$$
$$\left.+\frac{L}{2}\frac{1}{\sqrt{q(V_1+V_2)}\sqrt{1+\frac{E_a}{q(V_1+V_2)}}}\right], \tag{2.3}$$

where d_1 and d_2 are the distances between the first grid and the target and between the second grid and the first one, respectively; L is the length of the field-free region located between the second grid and the detector; V_1 and V_2 are electric potentials applied between grids and target (see Fig. 1).

The beam pulsation system having a time width of a few tens of ns does not provide a good enough time resolution to generate a precise start signal for the measurement of secondary ion TOFs. Assuming that prompt electrons are always emitted under a projectile impact, they are detected simultaneously (within 1 ns) such that the electron time signal can be used, event by event, as the origin of the time scale to determine the TOF of secondary ions. With this method the study is then restricted to negative secondary ions only. Typically, over a large number of events, the shape of the TOF peak for a given mass presents a smooth increase at low TOF values up to a maximum followed by a sharp linear decrease down to the peak origin, $t_0^{\exp}$, corresponding to the zero axial energy time value. One obtains a series of peak origins separated by a quantity proportional to $(\sqrt{m_i}-\sqrt{m_j})$, m_i and m_j

being masses of two different secondary ions. With a very accurate measurement of distances (d_1, d_2, and L) and voltages (V_1 and V_2) one calculates the value $t_0 = t(E_a = 0)$ given by Eq. (2.3). Thus, one can deduce the constant shift ($t_0^{\exp} - t_0$) to apply to TOF measurements in order to obtain their true value and then to build the corresponding axial energy distribution.

B. Radial energy determination

The radial energy E_r is directly correlated to the location of the secondary ion impact on the pixelated detector surface. This position is defined by X and Y coordinates with respect to the detector center (see Fig. 1) which corresponds to the intersection of the normal to the target—at the beam spot position—with the detector surface. Knowing the corresponding TOF t one can simply write

$$E_r = \frac{1}{2}m(V_X^2 + V_Y^2) = \frac{1}{2}m\left(\frac{X^2 + Y^2}{t^2}\right). \tag{2.4}$$

To determine experimentally the physical center of the detector we used, over a large number of events, the distribution of a given secondary ion impacts on the (16 $\times$ 16) pixels for different values of the acceleration voltage. The centroid value (X_c, Y_c) of such a distribution is expected to be the same whatever the applied voltage for secondary ions which are not preferentially emitted in a direction inclined with respect to the normal to the target surface. Systematic measurements were made over a large number of masses giving the (X_c, Y_c) value with an accuracy of 5%.

From the measurement of the axial and radial energies, one obtains for a given mass the total emission energy,

$$E = E_a + E_r. \tag{2.5}$$

It is worth pointing out that all the experimental kinematical quantities stem from the simultaneous measurements of TOF t and positions (X, Y) which depend on the acceleration parameters and on the characteristics of the detector used. As an example, to obtain a precise value of the axial energy E_a we used the double field method[11] which consists in applying a low acceleration voltage between the target and the first grid (typically V_1 was set to 1 kV with $d_1 = 1$ cm) and a higher voltage between the first and the second grids. This second voltage must be high enough to provide an efficient detection and collection of secondary ions ($V_2 = 9$ kV with $d_2 = 1$ cm). Over a large number of events, the experimental TOF distribution dN/dt of a given secondary ion mass is considerably broadened and the corresponding axial energy distribution $dNdE_a$ can thus be determined from Eq. (2.3) with a better accuracy.

C. Determination of experimental distributions

1. Principle of the analysis procedure

An event is defined as the impact of a projectile onto the target resulting in the emission of several secondary ions of different masses. For each secondary ion striking the pixelated detector, only the index number p of the hit pixel and the time t are recorded. With respect to the detector center, the position of each pixel is given by its center coordinates (X_p, Y_p) (see Fig. 1) but the precise impact coordinates of a secondary ion (X_i, Y_i) in the pixel area $(\Delta X \times \Delta Y)$ are not known experimentally and thus neither are the kinematical quantities (θ_i, ϕ_i, E_i). The time t is also measured within $\Delta t = 0.5$ ns, the time encoding bin width. Furthermore, experimental energy and angular distributions, defined as dN/dE and $dN/d\theta$, implicitly refer to constant dE and $d\theta$ intervals. Since axial and radial energies do not vary linearly with the raw data t, X, and Y [see Eqs. (2.3) and (2.4)] constant values of $d\theta$ and dE [see Eqs. (2.1) and (2.5)] are not straightforward to extract experimentally. A way to overcome these difficulties is to assign to each secondary ion impact coordinates (X_i, Y_i) within the pixel area and a time value t_i within Δt. Over a large number of events, the distribution of impact coordinates in a pixel as well as time values within Δt are assumed to be uniform. Thus, the values of X_i, Y_i, and t_i are chosen, event by event, through a random sampling procedure in the intervals $Xp \pm (\Delta X/2)$, $Yp \pm (\Delta Y/2)$, and $t \pm (\Delta t/2)$, respectively. From the set of values (X_i, Y_i, t_i) one deduces from Eqs. (2.1)–(2.5) the set of kinematical quantities (θ_i, ϕ_i, E_i) for each secondary ion. Experimental angular and energy distributions $dN/d\theta$ and dN/dE are then obtained by accumulating these quantities over a large number of events.

The important experimental conditions to validate this analysis procedure are the pixel size, the number of hit pixels and the number of events per pixel. It is therefore crucial to determine their influence on the quality of the final data.

2. Validity of the analysis procedure

In order to evaluate the validity of the procedure described above to extract the experimental distributions from the accumulated data, a complete simulation was made. We first assumed known angular and energy distributions of emitted particles defined by analytical expressions. This allowed us to simulate in well-defined experimental conditions trajectories and impacts of secondary ions on the detector for a sufficiently large number of events. In a second step we applied to the "theoretical" data collected by the 16 $\times$ 16 pixels detector (pixel by pixel) the overall random sampling procedure for recalculating the angular and energy distributions. The agreement between the initial theoretical distributions and the recalculated ones is a test of the method reliability.

For example, the energy distribution derived from the theoretical linear collision cascade sputtering model[5] was used,

$$\left(\frac{dN}{dE}\right)_e = a\frac{E}{(E + U_b)^n} \tag{2.6}$$

with U_b the surface binding energy and the exponent n varying from 2 to 3.[12]

If we consider an emission azimuthal symmetry with respect to the normal to the target surface, the azimuthal angle distribution is simply equal to a constant K,

$$\left(\frac{dN}{d\phi}\right)_e = K. \tag{2.7}$$

In that case, for simplification reasons, one can consider an angular distribution that follows a power law of cosine with no correlation with the energy, such as

$$\left(\frac{dN}{d\Omega}\right)_e \propto \cos^p \theta \tag{2.8}$$

and then

$$\left(\frac{dN}{d\theta}\right)_e = 2\pi \sin\theta \left(\frac{dN}{d\Omega}\right)_e = 2\pi \sin\theta \cos^p \theta \tag{2.9}$$

with θ the polar angle and p being typically between 1 and 2.

A set of values of $[(E)_e,(\phi)_e,(\theta)_e]$ is obtained by a random sampling taking into account these initial distributions given by Eqs. (2.6), (2.7), and (2.9). To simulate the detector response, one calculates the time $(t)_e$ and coordinates $[(X)_e,(Y)_e]$ corresponding to an impact of a given secondary ion onto the detector. The time $(t)_e$ is deduced from Eq. (2.3) by setting d_1, d_2, L, V_1, and V_2 equal to the experimental values, and using the axial energy value $(E_a)_e$ related to the emission energy $(E)_e$ by

$$(E_a)_e = (E)_e \cos^2(\theta)_e. \tag{2.10}$$

Coordinates $[(X)_e,(Y)_e]$ are obtained from the two components of the radial velocity given by

$$(V_X^2)_e = \frac{2}{m}(E_r)_e \cos^2(\phi)_e = \frac{(X^2)_e}{(t^2)_e}, \tag{2.11}$$

$$(V_Y^2)_e = \frac{2}{m}(E_r)_e \sin^2(\phi)_e = \frac{(Y^2)_e}{(t^2)_e}, \tag{2.12}$$

with

$$(E_r)_e = (E)_e \sin^2(\theta)_e. \tag{2.13}$$

To the position $[(X)_e,(Y)_e]$ is then associated a given hit pixel p of coordinates (X_p,Y_p). From the set $[X_p,Y_p,(t)_e]$ the analysis based on the random sampling described in Sec. II C 1 is then applied to obtain the recalculated energy and angular distributions. We have generated 10^6 events and the maximum energy $(E)_e$ was limited to 100 eV.

a. Energy distribution.

Figure 2 shows the good agreement obtained between the energy distribution recalculated with our method and the initial theoretical one using $n=2$ and $U_b=3.78$ eV (the heat sublimation for gold) in Eq. (2.6) for two different intervals of θ. The relative difference between the two curves is represented in the inset in both cases. Except for small energies (<1 eV), this difference does not exceed 5%. Therefore, even for small or large values of θ corresponding to a small number of hit pixels, the use of a uniform sampling within each pixel area does not modify the experimental energy distributions. One can also notice that the maximum energy is 90 eV for $10° < \theta < 20°$ [Fig. 2(a)] and only 20 eV for $50° < \theta < 60°$ [Fig. 2(b)]. This is due to the geometrical acceptance of the detector. In this simulation, only radial energies below 20 eV are detected (see further in Sec. III B).

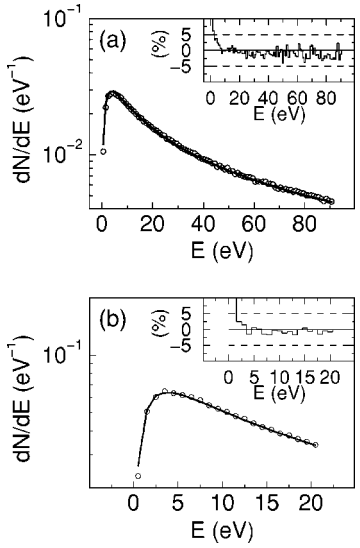

FIG. 2. (a) Comparison of energy distributions calculated (solid line) from Eq. (2.6), using $n=2$ and $U_b=3.78$ eV, and simulated (○) obtained through the procedure described in Sec. II C 2 with 16×16 pixels of area 2.54 mm$\times$2.54 mm, for a polar angle range $10° < \theta < 20°$ and with experimental parameters given in Fig. 1. In the inset is represented the relative difference (%) between the two curves. (b) Same as (a) for $50° < \theta < 60°$.

b. Angular distribution.

Good agreement also is obtained between the recalculated angular distribution and the theoretical one given by Eq. (2.8) with $p=2$ (see Fig. 3). A slight difference is however observed for the low energy interval ($0 < E < 3$ eV) as the

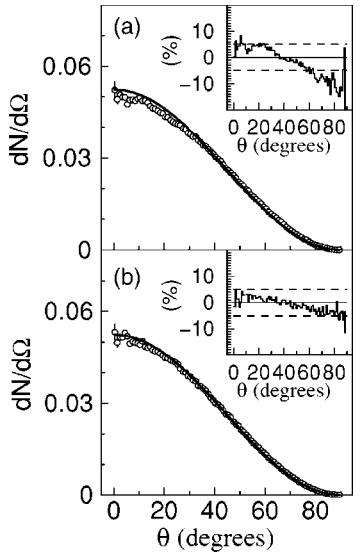

FIG. 3. (a) Comparison of angular distributions calculated (solid line) from Eq. (2.8), using $p=2$, and simulated (○) for an emission energy range 0 eV$< E <$3 eV according to the procedure described in Sec. II C 2 with the same experimental conditions as in Fig. 2. In the inset is represented the relative difference (%) between the two curves. (b) Same as (a) for 12 eV$< E <$15 eV.

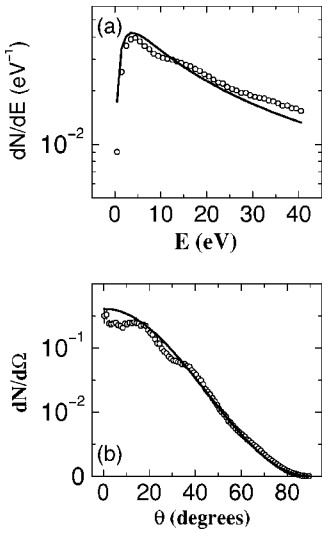

FIG. 4. (a) Comparison of energy distributions calculated (solid line) from Eq. (2.6), using $n=2$ and $U_b=3.78$ eV, and simulated (○) for a polar angle range $30° < \theta < 40°$ with 8×8 pixels of area 5.08 mm $\times$ 5.08 mm. The simulation procedure and the experimental parameters are the same as in Fig. 2. (b) Comparison of angular distributions calculated (solid line) from Eq. (2.8), using $p=2$, and simulated (○) for an emission energy range 12 eV $< E <$ 15 eV. Same conditions as above.

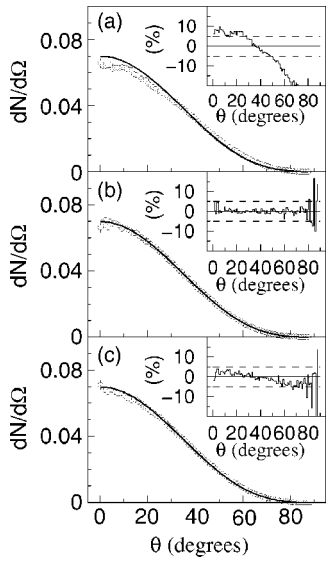

FIG. 5. (a) Comparison of angular distributions calculated (solid line) from Eq. (2.8), using $p=3$, and simulated (○) for an emission energy range 0 eV $< E <$ 3 eV with the same conditions as in Fig. 2. In the inset is represented the relative difference (%) between the two curves. (b) Same as (a) with 160×160 pixels of area 0.254 mm $\times$ 0.254 mm. (c) Same as (a) with the field-free region length extended to $L=80$ cm.

number of hit pixels is small. This is illustrated in Fig. 3(a) where the simulated angular distribution has smaller $dN/d\Omega$ values than the initial one at small θ angles since only few pixels near the detector center are hit. The relative difference does not exceed 5% for θ varying from 10° to 60° (see the inset). In contrast, theoretical and simulated $dN/d\Omega$ values are very similar for emission energies above 3 eV [see Fig. 3(b)]. Nevertheless, one can see in the insets of Fig. 3 that for $0° < \theta < 40°$ values of the theoretical $dN/d\Omega$ are systematically higher than values of the recalculated distribution and it is the opposite for $\theta > 40°$. Then, the exponent p obtained from the fit of the recalculated distribution is found to always be smaller—within a few percent—than the initial ones. For example, in Fig. 3(a) the exponent of the emission distribution is $p=2$ whereas the fit of the recalculated distribution gives $p=1.9$. Thus, one expects similar differences between the experimental angular distribution and the emission one that we want to determine. These differences have been taken into account in the analysis by correcting the emission parameters with an iterative procedure in such a way that the recalculated (using the method of Sec. II C 2) and experimental (using the method of Sec. II C 1) distributions coincide.

c. Pixel size effect.

As an illustration of pixel size effect, Figs. 4(a) and 4(b) display simulated energy and angular distributions for $30° < \theta < 40°$ and 12 eV $< E <$ 15 eV, respectively, with a detector having pixel area four times as large as the 16×16 pixels detector used in our experiments for the same total surface. The two curves are very different from the theoretical ones and "steps" in the distributions are observed because of the large pixel size. Then, it becomes difficult to fit the distributions using the theoretical expressions given by Eqs. (2.6) and (2.8), and thus to validate the proposed emission mechanisms. For very forward peaked distributions, the pixel size is also critical. An angular distribution with $p=3$ is shown in Fig. 5(a), with a regular 16×16 pixels detector, for 0 eV $< E <$ 3 eV. Reducing the pixel area by a factor 100 results in a very good agreement [see Fig. 5(b)]. But a similar improvement can be obtained with a 16×16 pixels detector by increasing the length L of the field-free region [see Fig. 5(c)]. In this case the secondary ions are of course spread over many more pixels because of the smaller detection solid angle.

From the comparison between known theoretical and recalculated distributions it is demonstrated that the proposed data analysis procedure gives a very satisfying agreement. This procedure can be thus applied to experimental data recorded by our 16×16 pixels detector provided that a sufficiently large number of pixels are hit and that the number of counts per pixel is high enough. When these conditions are fulfilled a careful fit of experimental energy and angular distributions allows us to determine the physical parameters involved in the emission mechanisms, and information can be also obtained on their relative contributions.

III. RESULTS

Three experiments have been performed using Au, Au_4 and Au_9 as projectiles at the same energy per atom, 200 keV, bombarding a gold target. The rate of emission of the various cluster ions depends on the size of projectiles. Only Au^- ion

TABLE I. List of analyzed secondary ions for each projectile.

Projectile	Analyzed secondary ions			
Au	Au^-			
Au_4	Au^-	Au_2^-	Au_3^-	
Au_9	Au^-	Au_2^-	Au_3^-	Au_5^-

emission has been observed with enough statistics when using Au projectiles. Although the statistics in the Au_4 experiment were the best it has only been possible to study the Au^-, Au_2^-, and Au_3^- emission; whereas, with Au_9 projectiles one obtained in addition the Au_5^- angular and energy distributions (see Table I).

Since kinematical quantities are measured event by event with the multianode detector, several types of correlations can be analyzed by processing the data off line.

A. Radial energy distribution

Experimentally the beam strikes the target at an angle of 45° with respect to the normal to the target in an horizontal plane perpendicular to its surface. A simple way to examine whether there is a favored emission direction for secondary ions is to compare their radial energy distributions dN/dE_r measured for ions detected in the left and right parts of the detector surface. Radial energies are defined positive in the (OX) direction and negative in the other one (see Fig. 1). Radial energy distributions of Au^-, Au_2^-, Au_3^-, and Au_5^- (normalized to unity) obtained with Au, Au_4, and Au_9 projectiles are shown in Figs. 6–8 for three different total energy intervals, $0\ \text{eV} < E < 5\ \text{eV}$, $5\ \text{eV} < E < 10\ \text{eV}$, and $10\ \text{eV} < E < 15\ \text{eV}$, respectively.

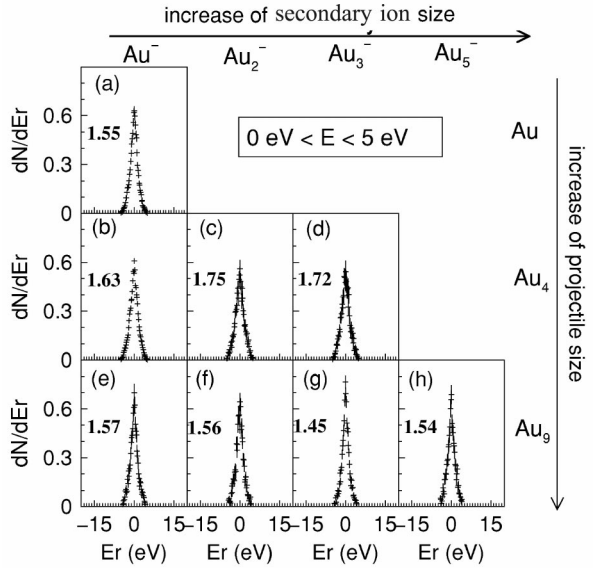

FIG. 6. Radial energy distributions dN/dE_r as a function of E_r for the total emission energy range $0\ \text{eV} < E < 5\ \text{eV}$. E_r is set positive for secondary ions detected in the right part of the detector in the (OX) direction and negative for the left part (see in Sec. III A). All radial energy distributions are normalized to unity and the standard deviation is given for each spectrum. Each figure [from (a) to (h)] presents the dN/dE_r of a given secondary ion (columns Au^-, Au_2^-, Au_3^-, and Au_5^-) for a given projectile (rows Au, Au_4, and Au_9).

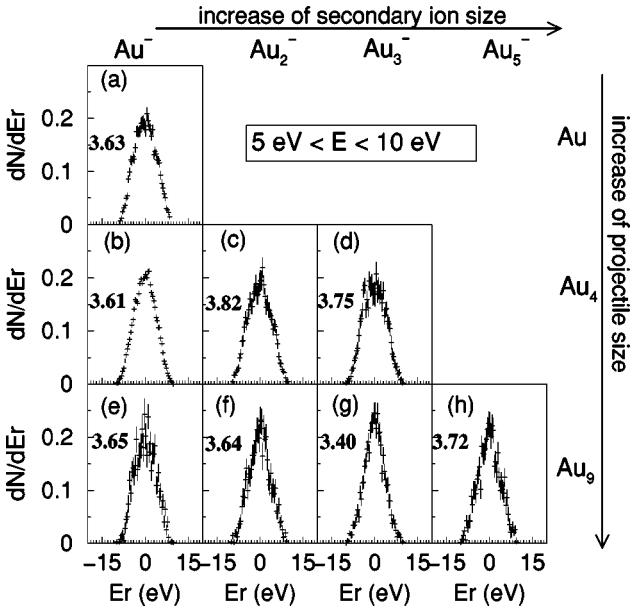

FIG. 7. Same as Fig. 6 for the emission energy range $5\ \text{eV} < E < 10\ \text{eV}$.

First, one can notice that the lower the emission energy the narrower the distributions, meaning that E_r increases with E. Furthermore, all these spectra are very symmetrical with respect to 0. Therefore, no favored emission direction is observed whatever the secondary ion type (up to an emission energy of 15 eV) and the projectile size. In addition, distributions resulting from impacts measured in the upper and the lower part of the detector surface [with respect to the (OX) direction] were also found to be similar which means that there is a rotational symmetry of the emission with respect to the normal to the target surface. Thus, it can be concluded that the memory of the primary beam direction is lost and that any emission mechanism model should reproduce this secondary ion symmetrical emission.

Nevertheless, the shapes of energy spectra shown in Figs. 6–8 depend on the type of projectiles and of secondary ions. For example, within a given energy range, radial energy distributions of Au^- ions emitted by Au, Au_4 or Au_9 projectiles are quite similar [see Figs. 6, 7, 8(a), 8(b), and 8(e)] while the width of Au_2^- and Au_3^- distributions decreases systematically with the projectile size [see (c) and (f), (d) and (g) in Figs. 6–8, respectively].

B. Angular distributions

Figure 9 displays the three-dimensional (3D) representation of the experimental distribution as a function of θ and E for Au^- secondary ions emitted with 200 keV/atom Au_4 projectiles. The values of θ and E are simply obtained for each event by the relations given in Secs. II A and II B using the time t and precise impact coordinates X_i, Y_i derived from the method described in Sec. II C 1. No assumption is thus made

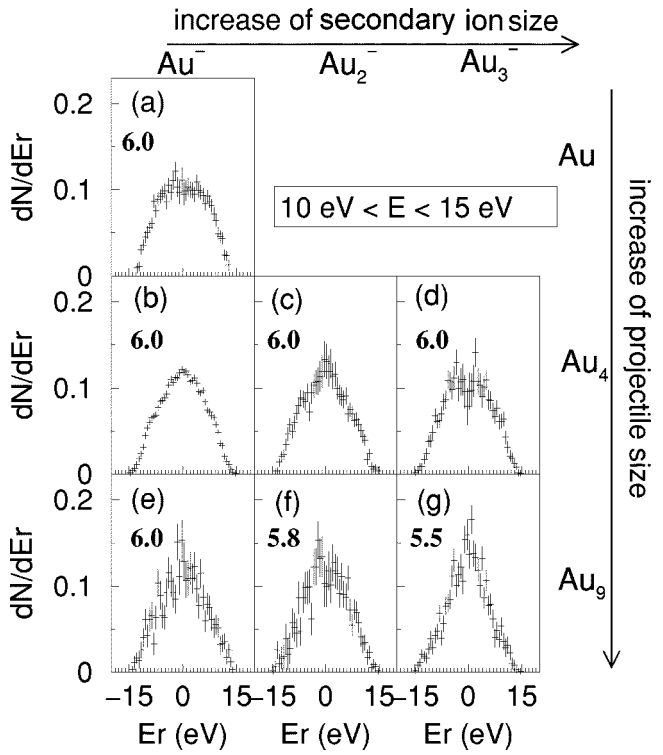

FIG. 8. Same as Fig. 6 for the emission energy range 10 eV $<E<15$ eV. (Because of low statistics the radial energy distribution of the Au_5^- secondary ion is not presented.)

on the type of secondary ion emission to build this 3D representation. Because of the geometrical acceptance of the detector, which depends on the applied voltages, the distance between the detector and the target, and the detector diameter, we cannot detect the secondary ions emitted from the target at large angles and energies. This is illustrated in Fig. 9 where it can be seen that secondary ions emitted at large polar angles ($\theta>70°$) are detected if their radial energy is smaller than 22 eV (in that case the total emission energy is close to the radial energy). By fixing the maximum detected radial energy $E_r^{\max}=22$ eV one can calculate the corresponding maximum emission angle $\theta^{\max}$ with the relation given by Eq. (2.1), $\tan\theta^{\max}=\sqrt{E_r^{\max}/E_a}$, for different values of the axial energy E_a varying from 0 to 100 eV. One can then associate to $\theta^{\max}$ the maximum emission energy, $E^{\max}=E_r^{\max}+E_a$. The pairs $(\theta^{\max},E^{\max})$ which are represented in the plane (θ,E) by black circles in Fig. 9 coincide with the experimental acceptance limit. The value of $E_r^{\max}$ is around 20 eV and 16 eV for Au and Au_9 experiments, respectively.

From a 3D spectrum $(\theta,E,d^2N/dEd\theta)$ as shown in Fig. 9, one can extract the $dN/d\theta$ distribution for different energy intervals. As the secondary emission is symmetrical with respect to the normal to the target, the angular distribution $dN/d\Omega$ can be obtained from experimental values $dN/d\theta$ by

$$\frac{dN}{d\Omega}=\frac{1}{2\pi\sin\theta}\frac{dN}{d\theta}. \tag{3.1}$$

Experimental distributions have been analyzed by the least square method and fitted by the power law $dN/d\Omega\propto\cos^p\theta$,

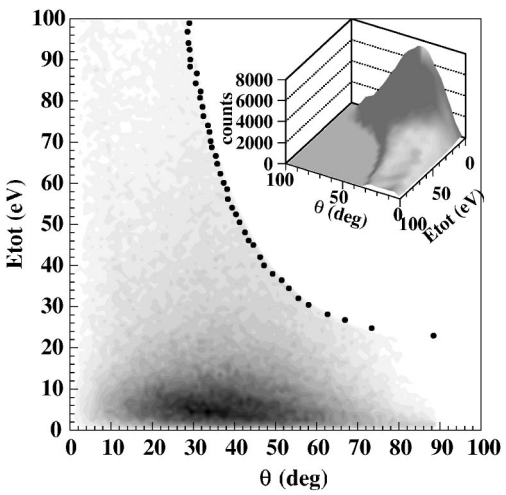

FIG. 9. 3D energy distribution of Au^- ions as a function of the emission angle θ obtained with Au_4 projectiles. The grey gradation represents the number of counts per channel as shown in the real 3D picture in the inset. The geometrical acceptance of the detector is represented by black circles (see Sec. III B).

usually used to reproduce the experimental sputtering angular distribution over the whole range of kinetic energies.[13,14] The analysis has been made using energy intervals of 3 eV from 0 to 15 eV. As an illustration, experimental and fitted curves for Au_2^- secondary ions and Au_4 projectiles are displayed for 0 eV$<E<$3 eV, 6 eV$<E<$9 eV, and 12 eV $<E<$15 eV in Figs. 10(a)–10(c), respectively. Figure 11 represents for all projectiles and detected secondary ions the value of the best fitting parameter p for each emission energy interval of 3 eV. It is observed that the exponent p increases as a function of the emission energy with a variation that depends on secondary ions and projectiles. The lowest energy component (0–3 eV) of the angular distributions follows systematically a less directional emission with $1.1<p<1.3$ (except for Au_3^- which has $p\sim1.5$) than the high energy component where $p\geqslant1.8$. Indeed, it must be remembered that the larger the exponent p value the narrower the angular distribution, i.e., more peaked in the normal direction to the surface. Above 10 eV, the exponent p remains constant and this saturation value p_{sat} increases with the pro-

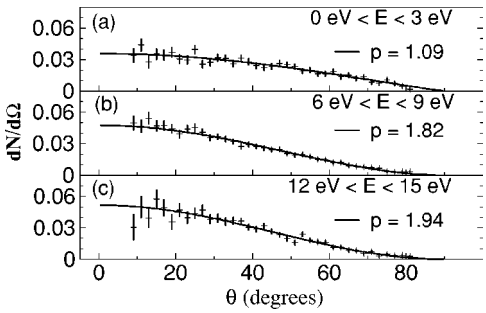

FIG. 10. Experimental angular distributions $dN/d\Omega$ of Au_2^- secondary ions with Au_4 projectiles for three different emission energy intervals. The exponent p value derived from the fit (solid line) using the distribution $dN/d\Omega\propto\cos^p\theta$ is given for each curve (see in Sec. III B).

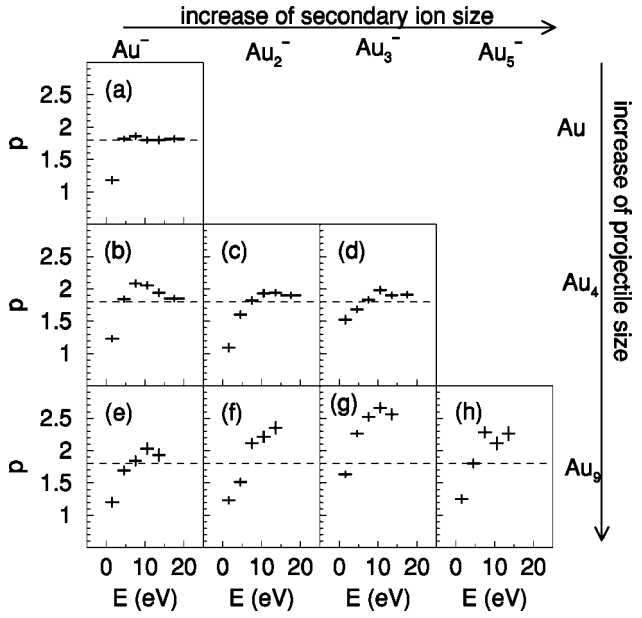

FIG. 11. Evolution of the exponent p (defined by $dN/d\Omega \propto \cos^p \theta$) as a function of the emission energy (see Sec. III B). Each figure [from (a) to (h)] represents the values of p for a given secondary ion (columns Au^-, Au_2^-, Au_3^-, and Au_5^-) and a given projectile (rows Au, Au_4, and Au_9). The horizontal dashed lines, corresponding to $p=1.8$, are guidelines for an easier comparison between the curves.

jectile size, it is close to 1.8 for Au^- secondary ions with Au projectiles [see Fig. 11(a)], around 2 with Au_4 projectiles [see Figs. 11(b)–11(d)] and with Au_9 projectiles, p_{sat} values are clearly higher than 2 for cluster secondary ions [see Figs. 11(f)–11(h)].

C. Energy distributions: analysis through the linear collision cascades and thermal spike mechanisms

From the (θ, E) correlations established in Sec. III B, the analysis of energy distributions must be made as a function of θ values. As shown above, Fig. 9 defines the experimental correlated limits of detection in angle and energy. For example, high energy secondary ions (up to 80 eV) can only be detected at angles between 10 and 30 degrees. Above 60° only secondary ions with energy smaller than 30 eV can be detected. Single energy distributions were derived from the experimental data for intervals $\Delta\theta$ of 10° (between 10° and 60°). It is thus possible to compare the dN/dE shapes as a function of θ ($10° < \theta < 20°, 20° < \theta < 30°, \ldots$).

In a previous analysis[15] only data obtained with Au_9 projectiles were available. We had tested the energy distribution proposed by Sigmund[6,16] by including a "spike volume" temperature T,

$$\frac{dN}{dE} = \alpha \frac{E}{(E+U_b)^2} \exp\left[-\left(\frac{E+U_b}{kT}\right)\right]. \quad (3.2)$$

In the framework of this model, the evolution of secondary ion energy spectra with θ is related to a change of the temperature and it has been possible to fit all the energy distributions of secondary ions from Au^- to Au_5^- provided we set the value of the surface binding energy U_b to (2.7±0.1) eV. This analysis clearly shows that the smaller the polar angle the larger the spike temperature, the value found for kT is around 40 eV for $20° < \theta < 30°$ and decreases down to 25 eV for $40° < \theta < 50°$.

However, this "spikelike" model is questionable as regarding data obtained with Au_4 projectiles. Indeed, the expression given by Eq. (3.2) does not fit the Au^- energy distributions and for U_b values smaller or close to the sublimation energy for gold it gives rise to a steeper slope at low emission energy which cannot reproduce the cluster energy spectra. Similar results are obtained for Au^- secondary ions with Au projectiles. As this model fails to describe the ion emission induced by Au and Au_4 projectiles, we have considered a different approach which separates clearly a linear collision cascade process from a conventional thermal spike phase.

Recently, MD simulations were performed to study energy and angular distributions of sputtered atoms from gold target bombarded by Au_2 projectiles at 100 keV/atom.[4] They show that energy distributions can be described by the linear cascade model in the early stage of the cascade for $t < 0.5$ ps, and by the thermal spike model for $t > 0.5$ ps. Experimentally, it is not possible to separate temporally these two mechanisms and we have attempted to reproduce the secondary ion energy distributions by summing the contribution of these two mechanisms according to the following expression:

$$\frac{dN}{dE} = a\frac{E}{(E+U_b)^n} + b\frac{E}{(kT)^{3/2}} \exp\left[-\left(\frac{E+U_b'}{kT}\right)\right]. \quad (3.3)$$

The ionization probability dependence on the type of emitted particles and on the size of the incident cluster is poorly known and we have thus assumed that the behavior of ionized species (in terms of energy and angular distributions) was similar to neutral entities. To fit experimental distributions, six parameters must be adjusted. The physical parameters are n, the surface binding energies U_b and U_b', and the effective temperature kT, that can only vary within certain limits. The two other parameters, a and b, are related to the relative contribution of each mechanism as described later. The exponent n is predicted by the linear collision cascade theory to vary between 2 and 3.[12] The binding energy U_b should remain close to the heat sublimation for gold (3.78 eV) for atomic emission. The effective binding energy U_b' in the Sigmund-Claussen model[6] is expected to be equivalent or smaller than U_b because of the increased damage to the target surface that could occur during the development of the thermal spike regime. Values of the effective temperature kT should remain below around 10 eV although it could be higher at the early stage of the spike. In a preliminary analysis, fits of energy spectra with free parameters have shown that the value of U_b' did not have much importance. Therefore, the results presented in the following have been obtained by fixing U_b' to 0 in order to reduce the number of parameters.

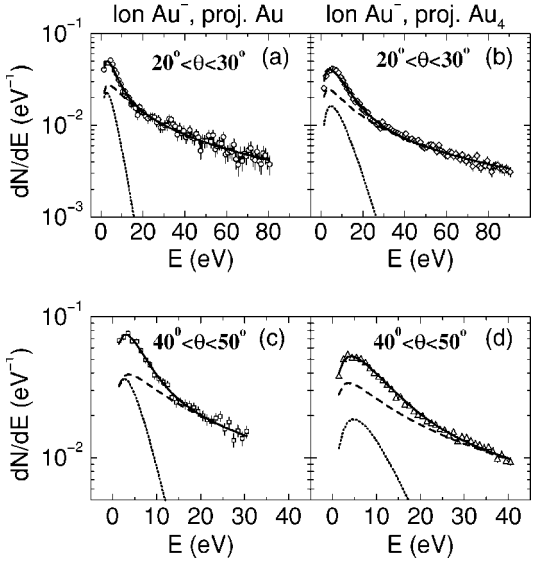

FIG. 12. (a) and (b) Experimental energy distributions of Au^- secondary ions obtained for $20° < \theta < 30°$ (○) and $40° < \theta < 50°$ (□) with Au projectiles. The solid lines are the fits using the energy distribution (LC+TS) given by Eq. (3.3) with parameters of Table II. (c) and (d) Experimental energy distributions of Au^- secondary ions obtained for $20° < \theta < 30°$ (◇) and $40° < \theta < 50°$ (△) with Au_4 projectiles. The solid lines are the fits using the energy distribution (LC+TS) given by Eq. (3.3) with parameters of Table III. The LC and TS energy contributions are represented by dashed and dotted lines, respectively.

1. Au projectile

With the monoatomic projectile Au, the high energy tail of the Au^- energy distribution suggests that its emission is mainly due to linear collision cascades. Experimentally, whatever the polar angle, the energy distributions are quite similar. Fits have been performed on energy spectra having the largest extension in energy and they are obtained for $10° < \theta < 20°$ and $20° < \theta < 30°$ [see Fig. 12(a)]. The value of the binding energy U_b increases very rapidly with n while the temperature remains rather constant. To maintain U_b close to 3.8 eV requires n to vary between 2 and 2.1 at this incident projectile velocity. With $n=2.05$ and $U_b=3.78$ eV, good fits are obtained with $kT=(2.6\pm0.2)$eV whatever the polar angle [see Figs. 12(a) and 12(b)]. By fixing the values of n, U_b, and kT, the slight variation of the energy distributions with the polar angle can be explained by a change in the proportion of the two mechanisms which is related to the parameters a and b in Eq. (3.3). As experimental energy spectra have been normalized to unity, one can deduce the contribution of each mechanism by integrating separately their corresponding energy distribution. At such a low effective temperature, the linear collision cascades (LC) govern the emission of Au^- secondary ions except for energy below few eV where the emission from a thermal spike (TS) becomes more important. For θ smaller than 40°, the contribution is around 82% for LC with a slight decrease of LC at larger angles (see Table II).

2. Au_4 *projectile*

Concerning the data obtained with Au_4 projectiles, the energy distributions of Au^-, Au_2^-, and Au_3^- have been fitted using $n=2.05$ as for Au projectiles since the energy per atom is the same.[12] The value of U_b giving the best agreement is also close to 3.8 eV but the temperature is higher than the one obtained with Au projectiles. For the Au^- ion kT is equal to 5 eV for $10° < \theta < 30°$ where energy spectra can be analysed up to 90 eV [see Figs. 12(c)] and remains constant with respect to the polar angle [see Figs. 12(d)]. The contributions of the two mechanisms are around 80% for LC and 20% for TS (see Table III) as with Au projectiles. These results indicate that within this approach the dominant process in the emission of the monomer with Au and Au_4 projectiles is linear collision cascades, and the increase of the projectile size causes an increase of the effective temperature.

TABLE II. With Au projectiles, values of the effective temperature kT and the relative proportions of linear collision cascades and thermal spike mechanisms, labelled by LC and TS, respectively, giving the best fits of Au^- secondary ions energy distributions using the (LC+TS) expression of Eq. (3.3). The fixed parameters are $n=2.05\pm0.05$ and $U_b=(3.8\pm0.3)$ eV.

Secondary ions	θ intervals	kT (eV)	LC (%)	TS (%)
Au^-	10°–40°	2.6±0.2	82±3	18±2
	40°–50°	2.6±0.2	76±2	24±1
	50°–60°	2.6±0.2	70±3	30±2

The shape of the Au_2^- and Au_3^- energy distributions is very different from the monomer. Good fits are obtained with $n=2.05$ and $U_b \sim 3.8$ eV, giving a value of kT close to 5 eV but the values of the parameters a and b change drastically. It is shown that the energy distributions of Au_2^- and Au_3^- are accounted for mainly by the thermal spike process (see Fig. 13). The largest contribution of the LC mechanism occurs for $20° < \theta < 30°$ where it represents around 35% of the Au_2^- emission. For higher values of θ it is only 25% (see Table III). For Au_3^-, the contribution of LC is constant with θ and is about 15% (see Table III).

3. Au_9 *projectile*

For this experiment, the small acceptance of the detector (the maximum detected radial energy is 16 eV) and the weak statistics limit the analysis to the range $20° < \theta < 50°$. As for Au and Au_4 projectiles we keep $n=2.05$ to fit energy distributions of the secondary ions Au^-, Au_2^-, Au_3^-, and Au_5^- obtained with Au_9 projectiles. Relatively good fits are obtained

TABLE III. Same as Table II with Au_4 projectiles and for Au^-, Au_2^-, and Au_3^- secondary ions energy distributions.

Secondary ions	θ intervals	kT (eV)	LC (%)	TS (%)
Au^-	10°–20°	5.0±0.2	83±2	17±1
	20°–60°	5.0±0.2	75±3	25±2
Au_2^-	20°–30°	5.0±0.2	35±5	65±5
	30°–60°	5.0±0.2	25±5	75±5
Au_3^-	20°–60°	5.5±0.2	18±5	82±3

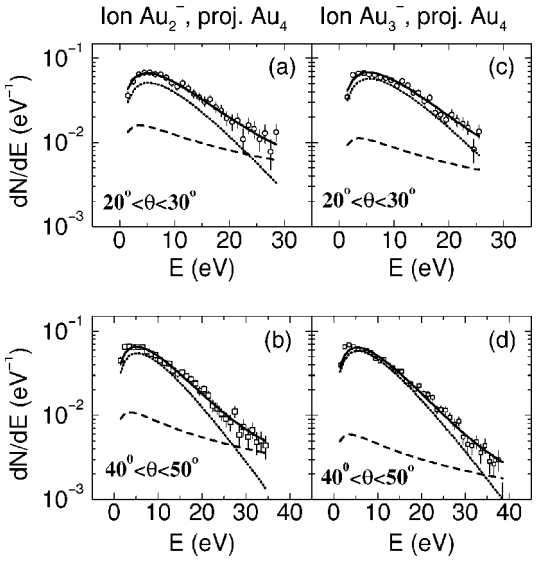

FIG. 13. (a) and (b) Experimental energy distributions of Au_2^- secondary ions obtained for $20° < \theta < 30°$ (○) and $40° < \theta < 50°$ (□) with Au_4 projectiles. The solid lines are the fits using the energy distribution (LC+TS) given by Eq. (3.3) with parameters of Table III. (c) and (d) Same as above for Au_3^- secondary ions. The LC and TS energy contributions are represented by dashed and dotted lines, respectively.

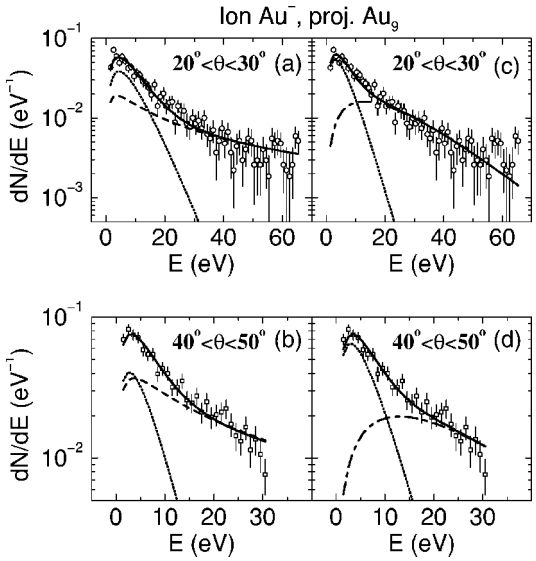

FIG. 14. (a) and (b) Experimental energy distributions of Au^- secondary ions obtained for $20° < \theta < 30°$ (○) and $40° < \theta < 50°$ (□) with Au_9 projectiles. The solid lines are the fits using the energy distribution (LC+TS) given by Eq. (3.3) with parameters of Table IV. The LC and TS energy contributions are represented by dashed and dotted lines, respectively. (c) and (d) In this case, the solid lines are the fits using the energy distribution (TS_h+TS_l) given by Eq. (4.1) with parameters of Table VI. The TS_h and TS_l energy contributions are represented by dotted-dashed and dotted lines, respectively.

with $U_b \sim 3.8$ eV for Au^- [see Figs. 14(a) and 14(b)] and clusters (see Fig. 15). However, the values of kT and the relative contributions of both mechanisms for cluster emission do not follow the trend expected from the data analysis of Au and Au_4 experiments as, for example, an increase of the effective temperature with the size of the projectiles. The kT value is found smaller than for Au_4 projectiles (see Table IV). For the Au^- ion there is a significant increase of the TS process in comparison with Au and Au_4 projectiles but it is surprising to observe that this process becomes much less important for the emission of Au_2^-, Au_3^-, and Au_5^- using Au_9 projectiles (see Table IV).

Another analysis has been performed with a lower binding energy, $U_b = 1.5$ eV, considering that Au_9 projectiles should induce more damage at the material surface. Good fits are also obtained and the values of the corresponding fitting parameters are summarized in Table V. In spite of a significant diminution of U_b, the effective temperature does not continue to increase with the size of the projectile and within this approach linear collision cascades are still the main process in the cluster emission (see Table V).

IV. DISCUSSION

The "spikelike" formula [see Eq. (3.2)] can only reproduce the energy distributions obtained with Au_9 projectiles, while a two step model consisting in a prompt emission of particles by the LC process followed by a "thermalized" emission seems to be much more appropriate for all types of incident Au_n projectiles provided that in the case of Au_9 projectiles the temporal evolution of the spike temperature is taken into account by an additional two step evaporation phase as shown later (see Sec. IV B).

To properly take into account the ionization probability in our description of the energy distributions of singly charged negative ions, simultaneous measurements of neutrals and/or positive secondary ions would be needed. We have thus assumed that the energy distribution given by Eq. (3.3) is also valid for ionized emitted species.

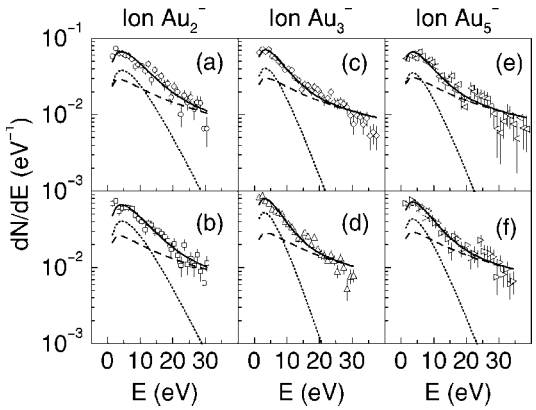

FIG. 15. With Au_9 projectiles, experimental energy distributions of Au_2^-, Au_3^-, and Au_5^- secondary ions (columns) obtained for $20° < \theta < 30°$ [row (a), (c), (e)] and $40° < \theta < 50°$ [row (b), (d), (f)]. The solid lines are the fits using the energy distribution (LC+TS) given by Eq. (3.3) with parameters of Table IV. The LC and TS energy contributions are represented by dashed and dotted lines, respectively.

TABLE IV. Same as Table II with Au_9 projectiles and for Au^-, Au_2^-, and Au_3^- secondary ions energy distributions.

Secondary ions	θ intervals	kT (eV)	LC (%)	TS (%)
Au^-	20°–40°	4.3±0.4	55±3	45±3
	40°–50°	2.7±0.4	70±3	30±2
Au_2^-	20°–40°	4.4±0.6	52±3	48±3
	40°–50°	4.4±0.6	49±3	51±3
Au_3^-	20°–40°	3.3±0.2	65±3	35±2
	40°–50°	3.3±0.2	57±3	43±3
Au_5^-	20°–40°	3.5±0.5	67±3	33±3
	40°–50°	3.5±0.5	59±3	41±3

A. Au and Au_4 projectiles

Concerning the five fitting parameters in Eq. (3.3) (a, U_b, n for the LC process, b and kT for the TS one) the value $n=2.05\pm0.5$, that we have kept constant for all Au_n projectiles as the incident energy per atom remains the same, has been initially fixed from the Au^- energy distributions with Au projectiles to obtain a value of the binding energy U_b close to the heat sublimation for gold (3.78 eV). With Au_4 projectiles, the values of U_b giving the best fit for the Au^- energy distributions is close to 3.8 eV and no dependence of U_b on the size of the emitted clusters has been clearly observed. Although the validity of keeping U_b constant can be questionnable, the analysis of the Au_2^- and Au_3^- energy distributions has shown that the LC process contributes weakly to their emission and thus the values of U_b do not significantly change neither the effective temperature nor the contributions of the LC and TS mechanisms.

The experimental value of the average effective temperature kT is close to the one given in Ref. 4 for 100 keV/atom Au_2 projectiles. It is observed that experimental angular distributions are less forward directed at low emission energy due to the TS process than at higher energy, which is also in agreement with these calculations. The increase of the TS contribution measured at large polar angles is consistent with this description. The fact that the emission of the Au^- secondary ion is mainly governed by linear collision cascade mechanism while clusters are preferentially emitted during the TS phase corroborates the results obtained with MD simulations on similar systems at lower bombarding energy.[3,17]

TABLE V. Same as Table IV with $U_b=1.5$ eV.

Secondary ions	θ intervals	kT (eV)	LC (%)	TS (%)
Au^-	20°–40°	4.8±0.2	64±3	36±2
	40°–50°	3.7±0.2	85±4	15±2
Au_2^-	20°–40°	5.7±0.3	45±3	55±3
	40°–50°	5.3±0.2	57±4	43±3
Au_3^-	20°–40°	5.2±0.4	68±3	32±2
	40°–50°	3.9±0.3	68±3	32±2
Au_5^-	20°–40°	6.5±0.2	56±3	44±3
	40°–50°	5.1±0.3	68±3	32±2

B. Au_9 projectiles

In the case of Au_9 projectiles the analytical description in terms of linear collision cascades and thermal spike processes shows that the TS contribution is much reduced in the cluster emission in comparison with Au_4 results. This suggests that fast processes remove a relatively large amount of energy in the early phase of the interactions when large size cluster projectiles are used. Dense collision cascades develop very quickly after simultaneous impacts of a large number of atoms. According to the temperature and the pressure existing in the core of the collision cascade, which depend on the deposited energy density, different scenarios of matter ejection take place, as flow of hot liquid at the surface, gasification or microexplosion[18–20] leading to a motion of the atoms and clusters as a "jetlike." For Au_9 projectiles, linear collision cascades as described by the Thompson formula[5] are unlikely to be the process responsible for high energy particles ejection. The large contribution of linear collision cascades is also ruled out by the very strong nonlinear effects observed experimentally in total sputtering[1] and secondary ion emission[21] induced by cluster projectiles at the same energy of 200 keV/atom. Furthermore, it was shown in the experimental angular distributions that the high energy component of energy distributions is more forward peaked than with Au and Au_4 projectiles [see Figs. 11(f)–11(h)]. This also indicates that the mechanism involved in the high energy particle emission with Au_9 projectiles leads to a more directional emission than with linear collision cascades. A single thermal spike phase with a temperature independent of time is not satisfying either since the temperature decreases as the energy density decreases. Then, following the approach of a two step emission mechanism we have first assumed that the high energy particles could be emitted during a hot spike regime corresponding to the very first piscoseconds of the explosionlike process. The more thermalized second phase would then occur later. Therefore, we have tried to fit the entire energy spectra by a sum of two Sigmund-Claussen distributions, the first one (TS_h) with an high average effective temperature kT_h, responsible for the high energy emission and the second (TS_l) with kT_l to reproduce the low energy part of energy spectra as with Au and Au_4 projectiles,

$$\frac{dN}{dE} = b\frac{E}{(kT_l)^{3/2}}\exp\left[-\left(\frac{E}{kT_l}\right)\right] + c\frac{E}{(kT_h)^{3/2}}\exp\left[-\left(\frac{E}{kT_h}\right)\right]. \tag{4.1}$$

As shown in Fig. 16, this expression reproduces quite well the energy distributions of clusters. The high and low effective temperatures are $kT_h \sim 8$ eV and $kT_l \sim 2.5$ eV, respectively. It is worth pointing out that the value of kT_l is similar to the one found for Au projectiles in the (LC+TS) description. The contributions of these two distributions, TS_h and TS_l, are found to be rather equivalent for all clusters and the slight increase of energy spectra slope with θ can be related to the diminution of the TS_h component (see Table VI). Concerning Au^- secondary ions, reasonably good fits are also obtained [see Figs. 14(c) and 14(d)] except at high energy (>55 eV) for small polar angles where the fitting curve deviates from the experimental one [see Fig. 14(c)]. The high

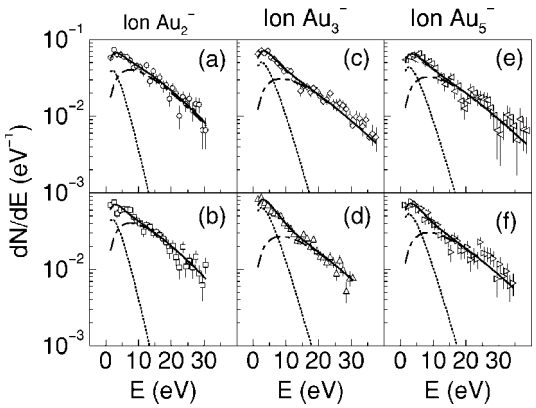

FIG. 16. Same as in Fig. 15. The solid lines are the fits using the energy distribution (TS_h+TS_l) given by Eq. (4.1) with parameters of Table VI. The TS_h and TS_l energy contributions are represented by dotted-dashed and dotted lines, respectively.

effective temperature kT_h is around 13 eV which is higher than for the cluster emission whereas kT_l is found to be similar. This could suggest that the single TS_h component would not be appropriate to reproduce the high energy tail of the Au^- energy distribution. It must be remembered that with Au_4 projectiles, the proportion of the LC process at low polar angles represents more than 80% of the monomer emission in contrast with clusters for which this process is much weaker (only ~25%). Thus, for Au_9 projectiles, one has attempted to fit the Au^- energy distribution for $20° < \theta < 30°$ by adding a third LC component to the expression given by Eq. (4.1) with U_b=3.78 eV and n=2.05, such as

$$\frac{dN}{dE} = a\frac{E}{(E+U_b)^n} + b\frac{E}{(kT_l)^{3/2}}\exp\left[-\left(\frac{E}{kT_l}\right)\right] + c\frac{E}{(kT_h)^{3/2}} \times \exp\left[-\left(\frac{E}{kT_h}\right)\right]. \quad (4.2)$$

A good agreement is obtained for $kT_h \sim 8$ eV and $kT_l \sim 2.5$ eV (see Fig. 17). The proportions of the three processes are (40±5)% for LC, (36±2)% for TS_h, and (24±2)% for TS_l. Unfortunately, it is not possible to apply the same fitting analysis for higher polar angles because the Au^- energy distributions are limited to around 30 eV. In the case of cluster energy spectra which also extend only to about 30 eV (see Fig. 16) the fits using Eq. (4.2) are therefore not possible either. Nevertheless, with Au_9 projectiles the LC process is still present and contributes significantly to the monomer emission, but this mechanism becomes negligible for clusters.

TABLE VI. With Au_9 projectiles, values of the high and low effective temperatures, kT_h and kT_l, respectively, and the relative proportions of the corresponding energy distribution labelled by TS_h and TS_l, giving the best fits of Au^-, Au_2^-, Au_3^-, and Au_5^- secondary ions energy distributions using the (TS_h+TS_l) expression of Eq. (4.1).

Secondary ions	θ intervals	kT_h (eV)	kT_l (eV)	TS_h (%)	TS_l (%)
Au^-	20°–30°	12.5±1	3.0±0.5	58±2	42±2
	30°–50°	12.5±1	3.0±0.5	50±2	50±2
Au_2^-	20°–40°	7.5±1	2.5±0.5	78±6	22±5
	40°–50°	7.5±1	2.5±0.5	71±4	29±4
Au_3^-	20°–40°	8.5±1	2.5±0.5	63±4	37±4
	40°–50°	8.5±1	2.5±0.5	56±5	44±5
Au_5^-	20°–40°	8.5±1	2.5±0.5	70±5	30±3
	40°–50°	8.5±1	2.5±0.5	60±4	40±4

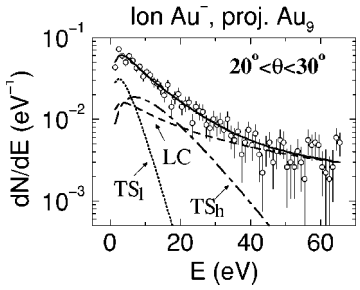

FIG. 17. With Au_9 projectiles, experimental energy distribution of Au^- secondary ions obtained for $20° < \theta < 30°$ (○). The solid line is the fit using the energy distribution (LC+TS_h+TS_l) given by Eq. (4.2) with the parameters n=2.05, U_b=3.78 eV, kT_h=8 eV, and kT_l=2.5 eV. The LC, TS_h, and TS_l energy contributions are represented by dashed, dotted-dashed and dotted lines, respectively.

C. MD simulations with 200 keV/atom Au_4 and Au_9 projectiles

The MD simulations reported in Ref. 4 investigated the temporal development of collision cascades following the bombardment of Au(111) targets with 100 keV/atom Au_2 ions. As noted previously the results suggested that the very early stage of the collision cascade was linear. However, the transition to a thermal spike occurred quickly. We have carried out additional simulations with 200 keV/atom Au_4 and Au_9 ions to see if the model used in Ref. 4 remains valid.

In these new simulations Au(111) targets again were used. The lateral target dimensions were kept the same as in Ref. 4, but target thickness was increased from 27 layers to 48 layers (65 952 atoms). A total of 18 impacts were simulated for both the 4-atom and 9-atom clusters. However, even with these thicker targets containment of the collision cascades was only fair owing to the much larger energy deposition (800 and 1800 keV for the 4-atom and 9-atom cluster, respectively, vs 200 keV in the earlier simulations).

In spite of the problem with collision cascade containment, the trends observed in these simulations are similar to those obtained in Ref. 4. The very early part of the collision cascades is well described by the linear cascade model, but after about 0.5 ps a thermal spike develops. In the simulations with 200 keV/atom Au_4 and Au_9 clusters, the linear cascade accounts for smaller fractions of the total yield. Because both the present simulations and the earlier simulations are cut off at 3 ps, only upper limits on the linear cascade contribution could be obtained. For the 4-atom cluster impacts the ratio of linear cascade to total yield is <2.3%, and for the 9-atom cluster impacts the ratio is <1.5% compared

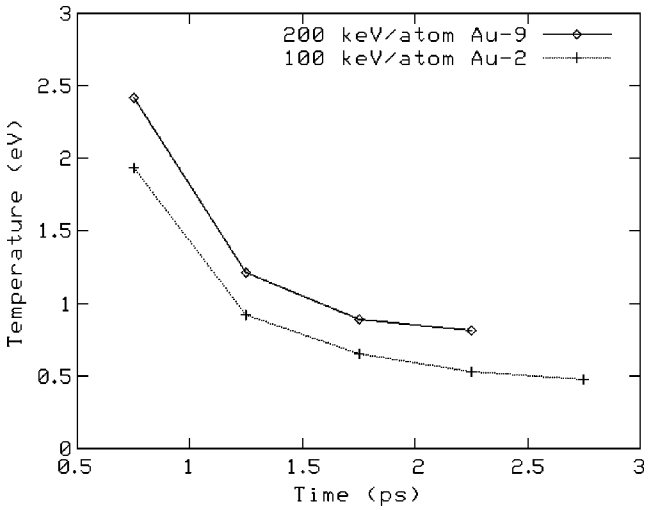

FIG. 18. Lower curve (+), effective collision cascade temperature versus time obtained in Ref. 4 for collision cascades following bombardment with 100 keV/atom Au_2 ions on Au(111) targets. Upper curve ($\diamond$), similar results for collision cascades following bombardment with 200 keV/atom Au_9 ions.

to a ratio that is $<3.4\%$ for the 100 keV/atom dimer impacts reported in Ref. 4.

As in the earlier simulations, the energy spectra of atoms ejected during the spike can be fit reasonably well with the Sigmund-Claussen model with an effective spike temperature that decreases fairly rapidly as the collision cascade ages. Figure 18 shows the effective cascade temperature vs time curves for both the Au_9 simulations and the earlier Au_2 simulations. As expected higher temperatures are seen with the 200 keV/atom Au_9 impacts; however, the difference between the two cases is not as large as might be expected owing to the containment problems experienced with the Au_9 impacts. This resulting artificial lowering of temperature with Au_9 ions should be even more pronounced for shorter times.

Although the conditions of the simulations do not correspond exactly to the experimental data reported in this paper (in the simulations fits are made to neutral atoms and clusters sputtered at all polar angles, while in the experiment single ions and ionized clusters are observed separately in restricted angular ranges), the simulation results are consistent with the experimental data. In particular, the energy spectra of ionized clusters—which generally are emitted later than single ions[17]—can be fit well with the Sigmund-Claussen model (with a decreasing effective spike temperature), while the fit to the energy spectrum of single ions (which includes more atoms ejected early in the collision cascade) requires a significant linear cascade component.

V. CONCLUSION

This work has shown that with high energy gold atoms and large clusters striking a gold target with an incident direction of 45° the secondary ion emission is symmetrical with respect to the normal to the surface. The most energetic particles are the most forward peaked and they correspond to fast emission processes.

A combination of linear collision cascades and spike models has been applied to reproduce the experimental energy distributions of atomic and cluster secondary ions emitted by Au and Au_4 projectiles. A large contribution of the thermal spike process is observed for the emission of cluster ions using Au_4 projectiles.

The analysis of the experimental data with Au_9 projectiles requires a different approach such as a fast collective process leading to the emission of the highest energy particles in the firt step of the interaction. Using the spike formula with two regimes of temperature allows us to reproduce the energy distributions of secondary ions with Au_9 projectiles.

To extend the present study to lower incident projectile energy would permit an easier comparison between experimental data and MD simulations. The use of a multipixel detector for simultaneous secondary ion detection is in that respect a very powerful tool.

ACKNOWLEDGMENTS

The authors are very grateful to L. Donadille for his precious help in performing the data analysis and for fruitful discussions. They would like also to thank L. Tassan-Got for his help and constant support. The involvement of A. Novikov in the experiments performed at the Tandem Accelerator at Orsay is greatly acknowledged.

[1] A. Brunelle, S. Della-Negra, J. Depauw, D. Jacquet, Y. Le Beyec, M. Pautrat, K. Baudin, and H. H. Andersen, Phys. Rev. A **63**, 022902 (2001).

[2] S. Bouneau, A. Brunelle, S. Della-Negra, J. Depauw, D. Jacquet, Y. Le Beyec, M. Pautrat, M. Fallavier, J. C. Poizat, and H. H. Andersen, Phys. Rev. B **65**, 144106 (2002).

[3] T. J. Colla and H. M. Urbassek, Nucl. Instrum. Methods Phys. Res. B **164–165**, 687 (2000).

[4] M. H. Shapiro and T. A. Tombrello, Nucl. Instrum. Methods Phys. Res. B **217**, 253 (2004).

[5] M. W. Thompson, Philos. Mag. **18**, 377 (1968).

[6] P. Sigmund and C. Claussen, J. Appl. Phys. **52**, 990 (1981).

[7] M. Benguerba, A. Brunelle, S. Della-Negra, J. Depauw, H. Joret, Y. Le Beyec, M. G. Blain, E. A. Schweikert, G. Ben Assayag, and P. Sudreau, Nucl. Instrum. Methods Phys. Res. B **62**, 8 (1991).

[8] Ch. Schoppmann, P. Wohlfart, D. Brandl, M. Sauer, Ch. Tomaschko, H. Voit, K. Boussofiane, A. Brunelle, P. Chaurand, J. Depauw, S. Della-Negra, P. Hakansosn, and Y. Le Beyec, Nucl. Instrum. Methods Phys. Res. B **82**, 156 (1993).

[9] S. Della-Negra, A. Brunelle, Y. Le Beyec, J. M. Curaudeau, J. P. Mouffron, B. Waast, P. Hakansson, B. U. R. Sundqvist, and E. S. Parilis, Nucl. Instrum. Methods Phys. Res. B **74**, 453 (1993).

[10] S. Bouneau, P. Cohen, S. Della Negra, D. Jacquet, J. Depauw, J.

Le Bris, M. Pautrat, and R. Sellem, Rev. Sci. Instrum. **74**, 57 (2003).
[11] M. Most, K. Wien, A. Brunelle, S. Della-Negra, J. Depauw, D. Jacquet, M. Pautrat, and Y. Le Beyec, Nucl. Instrum. Methods Phys. Res. B **168**, 203 (2000).
[12] P. Sigmund, Nucl. Instrum. Methods Phys. Res. B **27**, 1 (1987).
[13] H. H. Andersen, A. Johansen, and V. S. Touboltsev, Nucl. Instrum. Methods Phys. Res. B **164–165**, 727 (2000).
[14] G. Bräuer, D. Hasselkamp, W. Krüger, and A. Scharmann, Nucl. Instrum. Methods Phys. Res. B **12**, 458 (1985).
[15] S. Bouneau, S. Della-Negra, J. Depauw, D. Jacquet, and Y. Le Beyec, in *Proceedings of the 17th International Conference on the Application of Accelerators in Research and Industry, Denton, Texas, 2002*, edited by Jerome L. Duggan (University of North Texas, Denton, 2003), p. 767.
[16] P. Sigmund and M. Szymonski, Appl. Phys. A: Solids Surf. **A33**, 141 (1984).
[17] M. H. Shapiro and T. A. Tombrello, Surf. Sci. **453**, 143 (2000).
[18] K. T. Waldeer and H. M. Urbassek, Nucl. Instrum. Methods Phys. Res. B **73**, 14 (1993).
[19] K. Nordlund, J. Keinonen, M. Ghaly, and R. S. Averback, Nucl. Instrum. Methods Phys. Res. B **148**, 74 (1999).
[20] E. Salonen, K. Nordlund, and J. Keinonen, Nucl. Instrum. Methods Phys. Res. B **212**, 286 (2003).
[21] M. Fallavier, R. Kirsch, S. N. Morozov, J. C. Poizat, J. P. Thomas, and N. Wehbe, Phys. Rev. B **68**, 140102(R) (2003).